Nano Research

Open Access

Research Article

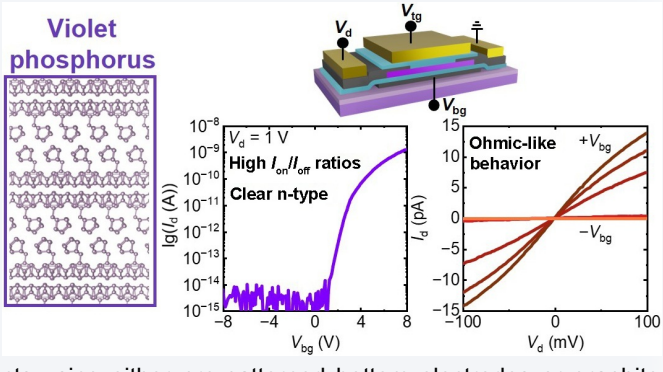
Robust n-type conduction with high on/off ratios in violet phosphorus field-effect transistors

Jae Joon Kim[1], Joonho Kim[1], Seoyoung Lim[2,3], Dong-gyu Kim[1], Uje Choi[1], Jieun Yeon[1], Jinsub Park[1], Dong-Wook Kim[2,3], and Kwanpyo Kim[1] ✉

[1] *Department of Physics, Yonsei University, Seoul 03722, Republic of Korea*
[2] *Department of Physics, Ewha Womans University, Seoul 03760, Republic of Korea*
[3] *Institute for Multiscale Matter and Systems (IMMS), Ewha Womans University, Seoul 03760, Republic of Korea*

Cite this article: *Nano Research*, **2026**, *19*, 94908865. https://doi.org/10.26599/NR.2026.94908865

ABSTRACT: Elemental phosphorus exhibits a rich polymorphism, and violet phosphorus (VP) has recently emerged as a layered semiconductor of interest for electronic and optoelectronic applications. However, its intrinsic charge-transport behavior has remained elusive, largely obscured by suboptimal device integration, low interface quality, and environmental degradation. Here, we report the fabrication and systematic characterization of multi-gate field-effect transistors based on high-quality VP crystals. To preserve the pristine nature of the channel, we employ a van der Waals (vdW) heterostructure architecture featuring full hexagonal boron nitride encapsulation and high-quality electrical contacts using either pre-patterned bottom electrodes or graphite contacts. Our devices exhibit robust n-type conduction with ohmic-like contact behavior, achieving I_{on}/I_{off} current ratios approaching 10^7 and long-term ambient stability. Notably, the n-type characteristics persist independent of the contact metal work function. Comprehensive dual-gate modulation and temperature-dependent analyses confirm clear unipolar n-type behavior of the VP channel. These findings clarify the inherent transport nature of VP and underscore the critical role of interface engineering in unlocking its full potential for advanced multifunctional electronic and optoelectronic devices.



KEYWORDS: violet phosphorus (VP), van der Waals (vdW) heterostructure, field-effect transistor (FET), n-type

1 Introduction

Elemental phosphorus allotropes have emerged as a significant class of materials, exhibiting a diverse range of electronic and optoelectronic properties that stem from their structural complexity and unique atomic configurations [1–8]. Among these, semiconducting phosphorus allotropes have attracted particular attention. Driven by their exceptional photoresponsivity and distinct electrical characteristics, these materials are being actively investigated as channel materials for high-performance field-effect transistors (FETs) and optoelectronic devices [9–12]. In particular, black phosphorus (BP) has been extensively studied as an archetypal 2D layered semiconductor, renowned for its high carrier mobility and ambipolar electrical behavior [13–15]. Similarly, other allotropes, such as amorphous (type-I) and fibrous (type-IV) red phosphorus (RP), have been reported to exhibit p-type electrical characteristics [12, 16–18]. Adding to this landscape of phosphorus semiconductors, violet phosphorus (VP, type-V) has garnered growing interest. VP possesses a layer-dependent bandgap, estimated to be approximately 2.5 eV for monolayer and 1.6 eV in bulk form [19, 20]. This property, combined with its strong photoresponsivity, makes it a promising candidate for phototransistor applications [21–23].

Despite these intriguing prospects, the fundamental charge transport nature of VP remains unclear. For instance, while some studies have suggested p-type behavior [21, 24], others have observed n-type characteristics [25, 26], indicating that the intrinsic transport mechanism is not yet fully elucidated. This lack of clarity is further compounded by the suboptimal performance of currently reported devices, which are frequently characterized by low I_{on}/I_{off} ratios and carrier mobilities that fall short of those observed in BP

Received: February 25, 2026; **Revised:** April 17, 2026
Accepted: May 22, 2026

✉Address correspondence to kpkim@yonsei.ac.kr

and RP. Furthermore, the persistent challenge of forming reliable, low-resistance ohmic contact continues to impede the realization of high-performance VP electronics.

To address these challenges and unveil the native charge transport properties of VP, we report the fabrication of high-performance FETs utilizing high-quality VP crystals. To mitigate the material's susceptibility to ambient degradation, all exfoliation and van der Waals (vdW) assembly procedures were strictly performed within an inert nitrogen-filled glovebox (O_2, H_2O < 0.1 ppm). Recognizing that conventional direct metal deposition processes are prone to inducing structural defects on the channel surface, we implemented damage-free contact strategies, utilizing vdW graphite contacts or pre-patterned metal bottom-contacts, to eliminate fabrication-induced defects and preserve the chemically pristine VP interface. Through this robust architecture, we successfully observed unambiguous n-type transport behavior with linear ohmic characteristics, providing compelling evidence to clarify the inherent conduction polarity of VP. These findings not only shed light on the native transport mechanism of VP but also demonstrate its significant potential for future electronic applications.

2 Methods

2.1 Synthesis of violet phosphorus crystals

A quartz tube, with dimensions of 30 cm in length, 15 mm in outer diameter, and 13 mm inner diameter, was prepared. Its interior was cleansed through sonication first in acetone and subsequently in isopropanol (IPA). Following the cleaning, the quartz tube was transferred into a glove box operating under a N_2 atmosphere. Within the environment, red phosphorus lumps (99.999%, Thermo Fisher Scientific), tin(IV) iodide (SnI_4, 99.999%, Sigma-Aldrich), and tin powder (Sn, 99.995%, Thermo Fisher Scientific) were sequentially loaded into the quartz tube. A quartz wool was inserted to approximately 18 cm of the tube. A quartz rod was then positioned on top of the wool. The tube was sealed under a high vacuum of 10^{-4} Torr at the location of the rod. The sealed ampule was then placed in a furnace. A heating gradient was established, and the synthesis was carried out for approximately 153 h. After the furnace cooled to ambient temperature, the ampule containing the synthesized crystal was transferred back into the glove box. The resulting violet phosphorus crystals were then carefully collected from the quartz ampoule.

2.2 Optical and structural characterization

We initially identified the exfoliated flakes utilizing an optical microscope (DM750, Leica). The approximate thickness of the VP flakes was estimated by analyzing the optical contrast in transmission mode. To verify the precise height and surface morphology of the flakes, we employed atomic force microscopy (AFM, XE-7, Park Systems). For detailed structural analysis, we prepared samples for electron microscopy by transferring VP flakes onto silicon nitride (Si_3N_4) transmission electron microscopy (TEM) grids via a polydimethylsiloxane (PDMS) stamp. This transfer process was conducted entirely within a nitrogen-filled glove box to prevent surface oxidation. We examined the flake morphology using SEM (JSM-7001F, JEOL) with an acceleration voltage of 10 kV. Additionally, SAED patterns were recorded using a TEM instrument (JEM-2100PLUS, JEOL) at 200 kV to assess the crystallinity. Finally, Raman spectroscopy measurements were performed using a system equipped with a 532 nm excitation laser (XperRAM, Nanobase) to further validate the crystal structure. KPFM measurements were performed using AFM (NX10, Park Systems) with Pt-coated Si probes (NSG01Pt, NT-MDT) at a scan rate of 0.35 Hz. For the sample, a graphite flake was transferred to make direct contact with the VP flake and bridge it to pre-deposited Ti/Au (10/50 nm) electrodes, serving as an electrical ground. All KPFM measurements were conducted in a nitrogen-purged environment with a relative humidity of 2%–4% and a temperature of 26–27 °C.

2.3 Device fabrication and characterization

To avoid ambient oxidation, the VP, graphite, and h-BN flakes were mechanically exfoliated inside a glove box. This process utilized adhesive tape and PDMS. The exfoliated flakes were subsequently dry-transferred onto Si/SiO_2 (300-nm-thick) substrates utilizing a PDMS stamp. For devices incorporating graphite-contact electrodes, patterning was performed using standard electron-beam lithography (PIONEER Two, Raith). This was followed by the deposition of Ti/Au (3/80 nm) in a thermal evaporator (15NNS004, NNS Vacuum). For the fabrication of pre-patterned bottom-contact devices, metal stacks of Ti/Au (2/20 nm) or Pt (20 nm) were employed as the contacts. Electrical characterization was conducted within a vacuum probe station (MS Tech). The measurements were performed under a high vacuum of approximately 10^{-3} Torr. A semiconductor parameter analyzer (Keithley 4200A SCS, Tektronix) was utilized for all data measurements.

3 Results and discussion

3.1 Structural and optical characterization of VP

VP crystals were synthesized utilizing a chemical vapor transport (CVT) method [27]. The detailed temperature profile and growth conditions are provided in the Electronic Supplementary Material (ESM) (Figs. S1 and S2 in the ESM). Figure 1 presents the crystal structural and optical analysis of the VP. The monoclinic crystal structure (space group *P*2/*n*) is illustrated in the side view (Fig. 1(a), *a*–*c* plane) and top view (Fig. 1(b), *a*–*b* plane) [19, 28]. The building block consists of distinct tubular structures formed by P_8 and P_9 cages which are interconnected by P_2 dumbbells [20]. The tubular building blocks form layered structure with perpendicular stacking fashion along the *c*-axis via vdW interactions, which facilitates the exfoliation of thin flakes. Optical microscopy images (Fig. 1(c)) reveal that the mechanically exfoliated flakes possess clean surface and exhibit distinct color contrasts determined by their thickness. This layer-dependent optical contrast is a critical feature that enables the visual identification and differentiation of flakes with varying layer numbers for device fabrication.

To rigorously evaluate the microscopic crystallinity, we transferred a representative VP flake onto a holey silicon nitride (Si_3N_4) grid for TEM analysis (Fig. 1(d)). The corresponding selected area electron diffraction (SAED) pattern shown in Fig. 1(e) displays a sharp and periodic rectangular array of diffraction spots. From this diffraction pattern, we were able to determine the crystallographic axes and identify the in-plane orientation of the VP flake [29]. Because VP preferentially tears along the tubular-strand direction, the exfoliated flakes are typically elongated along one in-

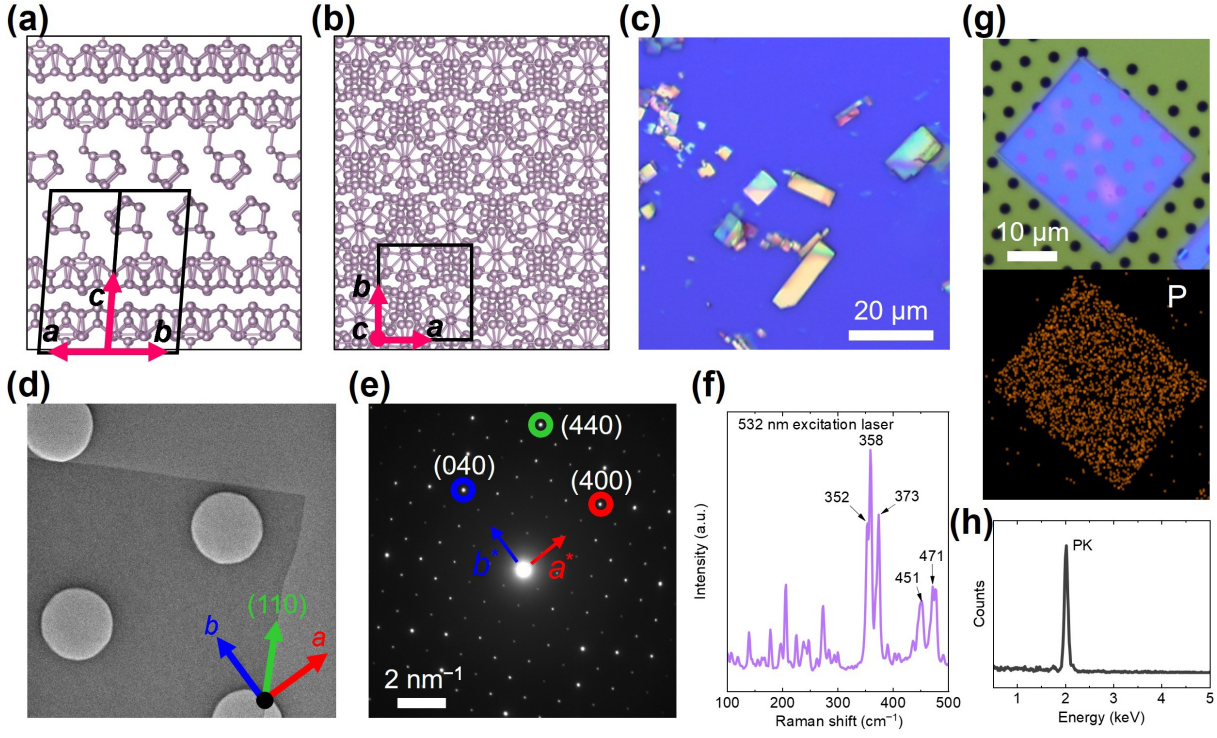


Figure 1 Structural and optical characterization of synthesized violet phosphorus (VP). (a) Side view and (b) top view of the monoclinic VP atomic structure (space group *P*2/*n*). The crystal axes are indicated by the red arrows. (c) Optical microscope image of exfoliated VP flakes on a SiO_2/Si substrate displaying layer-dependent color contrast. (d) TEM image of a VP flake transferred onto a holey Si_3N_4 grid. The red, blue, and green arrows indicate the *a*-axis, *b*-axis and (110) direction, respectively. (e) Selected area electron diffraction (SAED) pattern obtained from the flake. The colored circles correspond to (400), (040), and (440) diffraction spots. (f) Representative Raman spectrum of a VP flake acquired using a 532 nm excitation laser. (g) Optical image (top) and corresponding SEM-EDS elemental mapping of phosphorus (P) (bottom). (h) EDS spectrum verifying the high chemical purity of the synthesized VP crystals.

plane axis [20], and the channel length in this work was defined along this dominant elongated direction. Figure 1(f) shows a representative Raman spectrum acquired using a 532 nm excitation laser. The spectrum exhibits dominant peaks at 352, 358, 373, 451 and 471 cm^{-1}. These vibrational modes correspond to the stretching modes of the phosphorus cages and match well with the phonon signatures of monoclinic VP reported in previous literature [30]. Furthermore, the chemical purity was examined via scanning electron microscopy and energy-dispersive X-ray spectroscopy (SEM-EDS).

The elemental mapping in Fig. 1(g) demonstrates a homogeneous distribution of phosphorus throughout the flake. The accompanying EDS spectrum (Fig. 1(h)) reveals a distinct phosphorus peak with no detectable signals from oxygen or other impurities, indicating that the CVT-grown crystals are chemically clean and suitable for high-performance electronic devices. We note, however, that trace Sn/I-related residual species below the EDS detection limit cannot be completely excluded.

3.2 Electrical characteristics of VP FETs

To investigate the electrical properties of VP, we fabricated vdW heterostructure FETs. The device architecture is presented in the schematic diagram (Fig. 2(a)), and the corresponding optical image of a representative device is shown in Fig. 2(b). Detailed fabrication steps and atomic force microscopy (AFM) height profiles of the constituent flakes are provided in Figs. S3 and S4 in the ESM. To prevent fabrication-induced defects and environmental degradation, all exfoliation and dry-transfer procedures were conducted utilizing a polydimethylsiloxane (PDMS) stamp within a nitrogen-filled glove box where oxygen and moisture levels were maintained below 0.1 ppm. We employed a fully encapsulated structure using hexagonal boron nitride (h-BN) and graphite to seal the VP channel [31, 32]. Figure 2(c) plots the transfer curves I_d–V_{bg} measured at room temperature. The device exhibits distinct n-type conduction behavior where the drain current (I_d) increases systematically with positive back-gate voltage (V_{bg}), achieving a high I_{on}/I_{off} ratio exceeding 10^5. Notably, this n-type transfer behavior was consistently observed across multiple devices fabricated with similar structures, as demonstrated in Fig. S5 in the ESM, verifying the high reproducibility of our results. Corresponding output characteristics I_d–V_d shown in Fig. 2(d) further confirm this n-type nature. Notably, the linear dependence of current on voltage in the low-bias region (inset of Fig. 2(d)) indicates the formation of ohmic-like contacts between the VP channel and the graphite electrodes.

Beyond static performance, we investigated the long-term operational stability of the fully encapsulated VP devices. Figure 2(e) displays the time-dependent evolution of the normalized drain current I/I_0, where I_0 represents the current measured from the as-fabricated (day 1). The devices maintained their initial current levels with negligible degradation over an extended period. Furthermore, we assessed the environmental robustness by storing the devices in ambient air. As shown in Fig. 2(f), which tracks the evolution of transfer curves from the as-fabricated state to day 219, the devices exhibited remarkable resistance to oxidation and degradation. Key parameters such as the threshold voltage (V_{th}) and I_{on}/I_{off} ratio showed minimal deviation from their initial values even after prolonged air exposure.

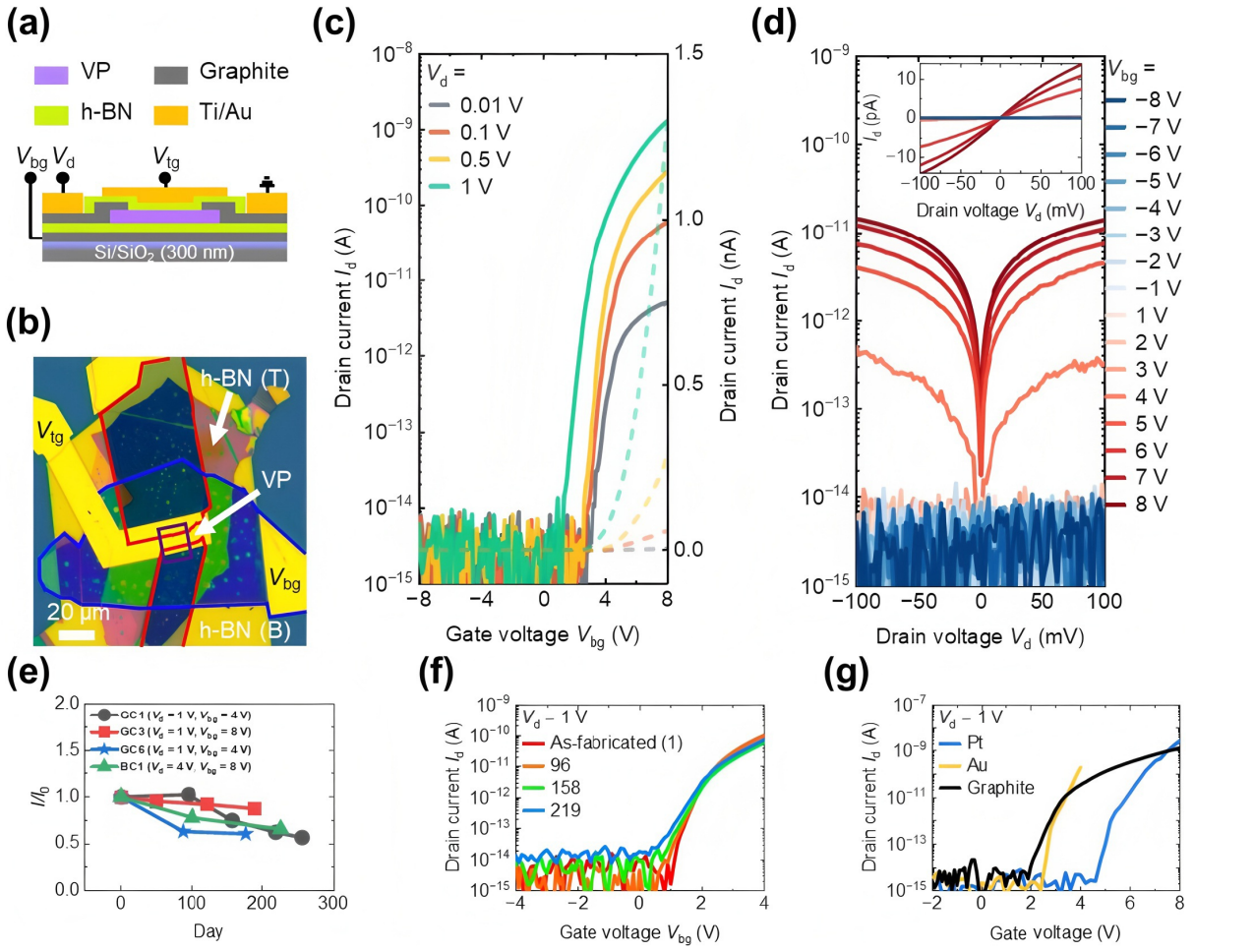


Figure 2 Electrical characteristics and environmental stability of VP FETs. (a) Schematic illustration of the h-BN encapsulated VP FET with graphite contacts. (b) Optical microscope image of a fabricated device. The white arrows indicate the top (T) and bottom (B) h-BN layers encapsulating the VP channel. The red and blue solid lines delineate graphite contact and graphite back-gate electrodes, respectively. (c) Transfer curve (I_d–V_{bg}) measured at various drain voltages (V_d). The solid and dashed curves represent the drain current (I_d) plotted on logarithmic (left axis) and linear (right axis) scales, respectively. (d) Output characteristics (I_d–V_d) at different gate voltages. The inset displays the linear curves in the low-bias region, indicating ohmic-like contact behavior. (e) Normalized drain current (I/I_0) of multiple devices monitored in ambient conditions for over 200 days. (f) Transfer curve comparison of a device under ambient storage. (g) Comparative transfer curves of VP FETs fabricated with different contact metals.

To verify the universality of the n-type behavior, we fabricated VP FETs using three different contact metals: graphite, Au, and Pt. To circumvent the channel degradation associated with conventional direct metal deposition, we adopted a damage-free integration strategy where VP flakes were dry-transferred onto the pre-patterned Ti/Au (2/20 nm) or Pt (20 nm) bottom-contacts. Figure 2(g) compares the transfer characteristics of these devices. Remarkably, all devices consistently exhibited distinct n-type electrical behavior regardless of the significant variation in contact metal work functions. In particular, VP devices with noble metal bottom-contacts demonstrated superior switching performance. The Au-contacted devices exhibited I_{on}/I_{off} ratios exceeding 10^6 (Fig. S6 in the ESM) and the Pt-contacted devices achieved ratios approaching 10^7. Figure S7 in the ESM presents a direct comparison of the electrical characteristics between these bottom-contact and conventional top-contacted VP devices. The extracted field-effect mobilities of the fabricated VP devices range from 10^{-3} to 10^{-1} cm^2/(V·s), with the highest value of 0.19 cm^2/(V·s) obtained from the representative device shown in Fig. S8 in the ESM. These results distinguish our work from existing studies, demonstrating not only the highest I_{on}/I_{off} ratio but also the most enduring environmental stability ever reported for VP FETs.

3.3 Temperature-dependent transport mechanism

To elucidate the fundamental charge transport mechanism governing the n-type behavior, we performed temperature-dependent electrical characterization of graphite-contacted devices from 293 to 373 K. Figure 3(a) presents the transfer curves measured at $V_{tg} = 1$ V across this temperature range. As the temperature rises, the on-state I_d increases monotonically while the off-state I_d remains largely unchanged. This thermally activated transport behavior is further evidenced in the output characteristics shown in Fig. 3(b). The device maintains excellent linearity in the low-bias region even at elevated temperatures (inset of Fig. 3(b)) which signifies that the robust ohmic-like contact is preserved. We analyzed this thermal activation using the thermionic emission model described by Eq. (1)

$$I_d \propto T^2 \exp(-q\Phi_B/k_B T) \quad (1)$$

where q is the elementary charge, Φ_B is the Schottky barrier height,

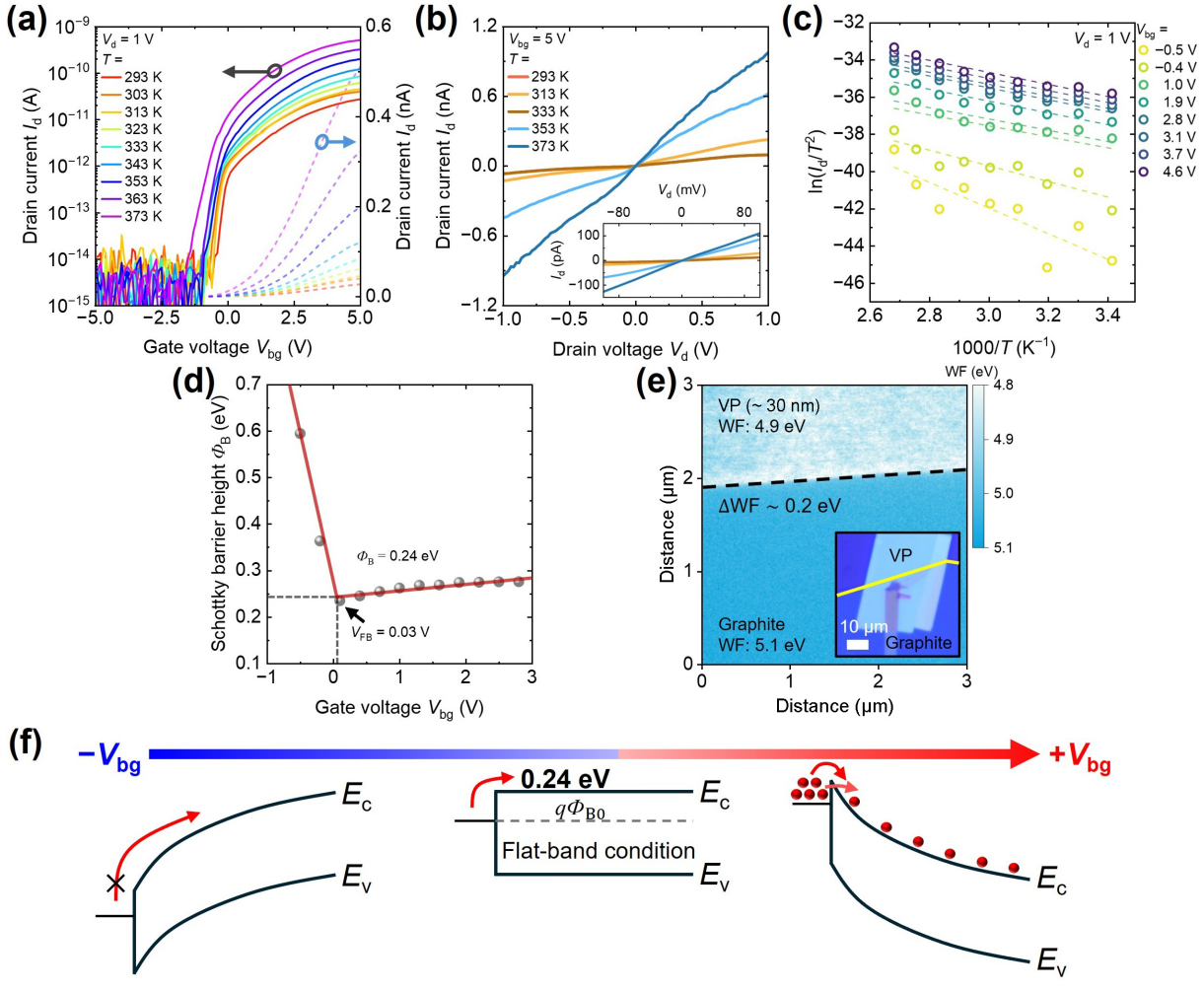


Figure 3 Temperature-dependent transport characteristics and analysis of the Schottky barrier. (a) Temperature-dependent transfer characteristics of a graphite-contact device measured from 293 to 373 K at V_d = 1 V. (b) Output characteristics at varying temperatures (V_{bg} = 5 V); the inset highlights the low-bias regime. (c) Arrhenius plots of $\ln(I_d/T^2)$ versus $1000/T$. (d) Extracted Schottky barrier height plotted as a function of V_{bg}. The inflection point corresponds to the flat-band voltage V_{FB}. (e) Work function (WF) map obtained via Kelvin probe force microscopy (KPFM), showing the WF difference between VP and graphite. (f) Schematic band diagrams illustrating the carrier transport mechanism under different gate bias conditions.

and k_B is the Boltzmann constant. Based on this relationship, we constructed Arrhenius plots of $\ln(I_d/T^2)$ versus $1000/T$ as displayed in Fig. 3(c). By extracting the slopes from these plots, we calculate the barrier height as a function of gate voltage (Fig. 3(d)). The flat-band voltage (V_{FB}) was determined to be 0.03 V and the Schottky barrier height at the graphite–VP junction was extracted to be approximately 0.24 eV.

To corroborate the electrically extracted barrier height with physical surface properties, we employed Kelvin probe force microscopy (KPFM) to map the surface potential [33]. Figure 3(e) presents the KPFM characterization of a graphite–VP heterostructure, where the work functions (WFs) of the VP (~ 30 nm thick) and graphite were measured to be 4.9 and 5.1 eV, respectively. The measured WF difference (ΔWF) of 0.2 eV agrees well with the electrically derived barrier height of 0.24 eV. Similar WF values were observed even in thicker VP flakes (~ 100 nm), as shown in Fig. S9 in the ESM. This consistency suggests that the junction properties are dominated by interface physics rather than bulk effects. Notably, our devices consistently exhibited n-type characteristics regardless of the contact metal work function (Pt, Au, or graphite). This unipolar behavior stands in distinct contrast to other phosphorus allotropes such as black phosphorus or red phosphorus which typically show p-type dominance. Such contact-metal-independent n-type transport is difficult to explain by a simple Schottky–Mott rule and instead suggests Fermi-level pinning by defect-derived surface/interfacial states near the conduction-band edge, likely associated with phosphorus vacancies and weak oxidation-related states [34, 35]. Consistent with this pinning model, Figure 3(f) schematically illustrates the corresponding band alignment under gate biasing. At negative gate voltages, the large Schottky barrier effectively blocks both electron and hole injection. Conversely, applying a positive gate bias induces downward band bending; this facilitates electron injection via the joint contribution of thermionic emission and tunneling, resulting in the observed n-type transport behavior.

3.4 Dual-gate structure modulation

We employed a dual-gate configuration to control the carrier density and further substantiate the n-type behavior. The dual-gated VP FET architecture featured a back-gate and a top-gate as depicted schematically in Fig. 4(a). By sweeping the V_{bg} while varying the V_{tg}, we obtained a 2D color map of the I_d a function of

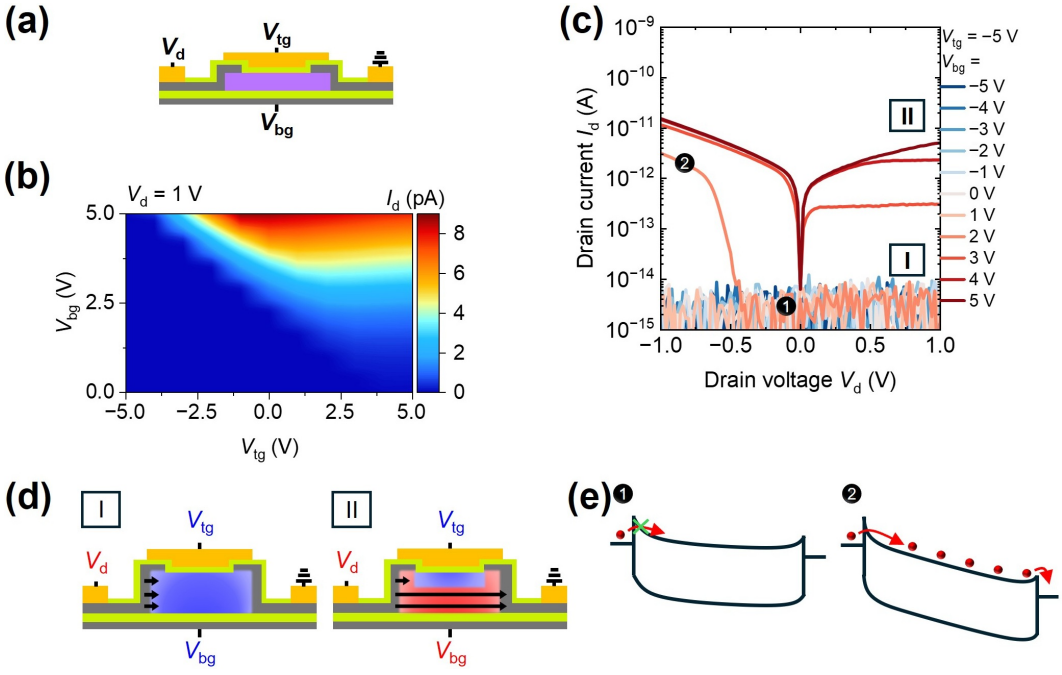


Figure 4 Dual-gate modulation and tunable carrier transport mechanism. (a) Schematic illustration of the dual-gate VP FET structure. (b) 2D color map of the transfer characteristics as a function of V_{bg} and V_{tg} plotted in a linear scale. (c) Output characteristics measured at a fixed $V_{tg} = -5$ V while varying V_{bg}. (d) Schematic representations of the channel condition corresponding to state I and state II as defined in (c). (e) Band diagrams corresponding to the specific bias points 1 and 2 marked in (c).

both V_{bg} and V_{tg} (Fig. 4(b)). As V_{tg} increases toward positive values, the V_{th} shifts negatively, indicating an electrostatic n-doping effect on the VP channel. Notably, under simultaneous negative biasing $V_{bg} < 0$ and $V_{tg} < 0$, the channel becomes completely off-state, and no hole transport is observed. This absence of a p-type branch, even under strong dual-gate modulation, further corroborates the robust unipolar n-type nature of our VP FETs (additional data in Fig. S10 in the ESM). Consistent dual-gate modulation behavior was also observed in devices with Au bottom-contacts as shown in Fig. S11 in the ESM.

Figure 4(c) displays the output characteristics measured under fixed $V_{tg} = -5$ V, which suppresses electron carriers without inducing p-type conduction. Consistent with the 2D color map, the device remains in the off-state (state I) when V_{bg} is negative value. As V_{bg} increases (state II), a conductive channel is formed, allowing carriers to flow. The schematic representations corresponding to these specific states are illustrated in Fig. 4(d). We specifically focus on the distinct transport behaviors marked by the black-circled numbers. At point 1 (low V_d region at $V_{bg} = 2$ V), the I_d is effectively suppressed due to the large Schottky barrier (left panel of Fig. 4(e)). In contrast, at point 2 (high negative V_d region at $V_{bg} = 2$ V), the device exhibits Schottky diode-like rectification. This current increase arises from the drain-induced Schottky barrier narrowing effect [36–38]. As depicted in the right panel of Fig. 4(e), the large drain field steepens the band bending at the drain contact, thereby facilitating carrier injection via tunneling [39–41]. Similar trends were observed.

Consequently, by modulating the gate and drain biases, the transport characteristics of our VP FETs can be continuously tuned. The operation evolves from a rectifying Schottky-diode-like behavior to a symmetric Ohmic-like regime. In the rectifying state, a rectification ratio of approximately 10^2 was observed. This versatile tunability highlights the potential of VP FETs as multi-functional devices capable of operating on distinct modes depending on the biasing conditions.

4 Conclusion

In summary, we successfully synthesized high-quality violet phosphorus single crystals via chemical vapor transport and integrated them into vdW heterostructure field-effect transistors. Crucially, our comprehensive electrical characteristics revealed robust n-type transport behavior, clarifying the previous ambiguous conduction polarity of the VP. The devices consistently exhibited unipolar n-type behavior regardless of the contact metal work function, highlighting the n-type nature of the material. By implementing damage-free graphite contact, pre-patterned bottom-contact strategy, and full encapsulation, we effectively minimized interface degradation. Consequently, we achieved a record-high I_{on}/I_{off} ratio approaching 10^7 and confirmed exceptional long-term environmental stability. Furthermore, we demonstrated that the transport characteristics can be tuned from a rectifying Schottky-diode regime to a symmetric Ohmic-like state via gate and drain bias modulation. These findings provide a clear understanding of the inherent transport properties of VP and suggest promising avenues for its application in next-generation multi-functional electronics.

Electronic Supplementary Material: Supplementary material (additional data regarding CVT synthesis, AFM profiles, and electrical characterization) is available in the online version of this article at https://doi.org/10.26599/NR.2026.94908865.

Data availability

All data needed to support the conclusions in the paper are presented in the manuscript and the Electronic Supplementary

Material. Additional data related to this paper may be requested from the corresponding author upon request.

Acknowledgements

This work was supported by the National Research Foundation of Korea (NRF) grant funded by the Korea government (MSIT) (No. RS-2025-00560649), the Global Learning & Academic Research Institution for Masters, PhD students, and Postdocs (G-LAMP) Program of the National Research Foundation of Korea, grant funded by the Ministry of Education (No. RS-2024-00442483), the National Research Foundation of Korea (NRF) grant funded by the Korea government (MSIT & MOE) (No. RS-2025-16063688), and K-CHIPS (Korea Collaborative & High-tech Initiative for Prospective Semiconductor Research) funded by the Ministry of Trade, Industry and Resources (MOTIR, Korea) (No. RS-2026-25521881).

Declaration of competing interest

All the contributing authors report no conflict of interests in this work.

Author contribution statement

J. J. K. and K. K. conceived the project and designed the experiments. J. J. K. and D.-g. K. synthesized the violet phosphorus crystals. J. J. K. fabricated the VP field-effect transistors and performed electrical measurements. J. K. and U. C. assisted with electron-beam lithography processes. S. L. and D.-W. K. conducted KPFM measurements. J. Y. performed TEM analysis, and J. P. carried out SEM and EDS characterizations. J. J. K. wrote the manuscript. K. K. supervised the entire project and acquired the funding. All authors participated in the scientific discussion and contributed to the writing of the manuscript.

Use of AI statement

None.

References

[1] Chowdhury, C.; Datta, A. Exotic physics and chemistry of two-dimensional phosphorus: Phosphorene. *J. Phys. Chem. Lett.* **2017**, *8*, 2909–2916.

[2] Ruck, M.; Hoppe, D.; Wahl, B.; Simon, P.; Wang, Y. K.; Seifert, G. Fibrous red phosphorus. *Angew. Chem., Int. Ed.* **2005**, *44*, 7616–7619.

[3] Zhang, J. L.; Zhao, S. T.; Han, C.; Wang, Z. Z.; Zhong, S.; Sun, S.; Guo, R.; Zhou, X.; Gu, C. D.; Yuan, K. D. et al. Epitaxial growth of single layer blue phosphorus: A new phase of two-dimensional phosphorus. *Nano Lett.* **2016**, *16*, 4903–4908.

[4] Sofer, Z.; Sedmidubský, D.; Huber, Š.; Luxa, J.; Bouša, D.; Boothroyd, C.; Pumera, M. Layered black phosphorus: Strongly anisotropic magnetic, electronic, and electron-transfer properties. *Angew. Chem., Int. Ed.* **2016**, *55*, 3382–3386.

[5] Lee, S.; Lee, Y.; Ding, L. P.; Lee, K.; Ding, F.; Kim, K. Atomically sharp, closed bilayer phosphorene edges by self-passivation. *ACS Nano* **2022**, *16*, 12822–12830.

[6] Yoon, J. Y.; Lee, Y.; Kim, D. G.; Oh, D. G.; Kim, J. K.; Guo, L. S.; Kim, J.; Choe, J.; Lee, K.; Cheong, H. et al. Type‐II red phosphorus: Wavy packing of twisted pentagonal tubes. *Angew. Chem., Int. Ed.* **2023**, *62*, e202307102.

[7] Lee, K.; Lee, S.; Lee, Y.; Kim, K. Deep learning analysis of localized interlayer stacking displacement and dynamics in bilayer phosphorene. *Adv. Mater.* **2025**, *37*, 2416480.

[8] Choi, Y. W.; Lee, Y.; Kim, K.; Zettl, A.; Cohen, M. L. Atomic and electronic structures of 1D phosphorus nanoring and nanohelix. *ACS Nano* **2025**, *19*, 12155–12160.

[9] Engel, M.; Steiner, M.; Avouris, P. Black phosphorus photodetector for multispectral, high-resolution imaging. *Nano Lett.* **2014**, *14*, 6414–6417.

[10] Youngblood, N.; Chen, C.; Koester, S. J.; Li, M. Waveguide-integrated black phosphorus photodetector with high responsivity and low dark current. *Nat. Photon.* **2015**, *9*, 247–252.

[11] Chen, X. L.; Lu, X. B.; Deng, B. C.; Sinai, O.; Shao, Y. C.; Li, C.; Yuan, S. F.; Tran, V.; Watanabe, K.; Taniguchi, T. et al. Widely tunable black phosphorus mid-infrared photodetector. *Nat. Commun.* **2017**, *8*, 1672.

[12] Smith, J. B.; Hagaman, D.; DiGuiseppi, D.; Schweitzer-Stenner, R.; Ji, H. F. Ultra-long crystalline red phosphorus nanowires from amorphous red phosphorus thin films. *Angew. Chem., Int. Ed.* **2016**, *55*, 11829–11833.

[13] Das, S.; Demarteau, M.; Roelofs, A. Ambipolar phosphorene field effect transistor. *ACS Nano* **2014**, *8*, 11730–11738.

[14] Li, L. K.; Yu, Y. J.; Ye, G. J.; Ge, Q. Q.; Ou, X. D.; Wu, H.; Feng, D. L.; Chen, X. H.; Zhang, Y. B. Black phosphorus field-effect transistors. *Nat. Nanotechnol.* **2014**, *9*, 372–377.

[15] Yang, F. Y.; Zhang, Z. C.; Wang, N. Z.; Ye, G. J.; Lou, W. K.; Zhou, X. Y.; Watanabe, K.; Taniguchi, T.; Chang, K.; Chen, X. H. et al. Quantum Hall effect in electron-doped black phosphorus field-effect transistors. *Nano Lett.* **2018**, *18*, 6611–6616.

[16] Amaral, P. E. M.; Nieman, G. P.; Schwenk, G. R.; Jing, H.; Zhang, R.; Cerkez, E. B.; Strongin, D.; Ji, H. F. High electron mobility of amorphous red phosphorus thin films. *Angew. Chem., Int. Ed.* **2019**, *58*, 6766–6771.

[17] Sun, Z. J.; Zhang, B. W.; Zhao, Y. K.; Khurram, M.; Yan, Q. F. Synthesis, exfoliation, and transport properties of quasi-1D van der Waals fibrous red phosphorus. *Chem. Mater.* **2021**, *33*, 6240–6248.

[18] Sun, Z. J.; Chen, W. J.; Zhang, B. W.; Gao, L.; Tao, K. Z.; Li, Q.; Sun, J. L.; Yan, Q. F. Polarization conversion in bottom-up grown quasi-1D fibrous red phosphorus flakes. *Nat. Commun.* **2023**, *14*, 4398.

[19] Schusteritsch, G.; Uhrin, M.; Pickard, C. J. Single-layered Hittorf's phosphorus: A wide-bandgap high mobility 2D material. *Nano Lett.* **2016**, *16*, 2975–2980.

[20] Zhang, L. H.; Huang, H. Y.; Zhang, B.; Gu, M. Y.; Zhao, D.; Zhao, X. W.; Li, L. R.; Zhou, J.; Wu, K.; Cheng, Y. H. et al. Structure and properties of violet phosphorus and its phosphorene exfoliation. *Angew. Chem. Int. Ed.* **2020**, *59*, 1074–1080.

[21] Ricciardulli, A. G.; Wang, Y.; Yang, S.; Samorì, P. Two-dimensional violet phosphorus: A p-type semiconductor for (opto)electronics. *J. Am. Chem. Soc.* **2022**, *144*, 3660–3666.

[22] Liu, X. X.; Wang, S. Y.; Di, Z. Y.; Wu, H. Q.; Liu, C. S.; Zhou, P. An optoelectronic synapse based on two‐dimensional violet phosphorus heterostructure. *Adv. Sci.* **2023**, *10*, 2301851.

[23] Chen, W. L.; Chen, A.; Zhang, R.; Zeng, J. M.; Zhang, L. H.; Gu, M. Y.; Wang, C. F.; Huang, M. Y.; Guo, Y. B.; Duan, H. X. et al. Strong in-plane optoelectronic anisotropy and polarization sensitivity in low-symmetry 2D violet phosphorus. *Nano Lett.* **2023**, *23*, 10821–10831.

[24] Zhai, R.; Wen, Z. R.; Zhao, X. W.; She, J. Y.; Gu, M. Y.; Bu, F. Q.; Huang, C.; Meng, G. D.; Cheng, Y. H.; Zhang, J. Y. Violet arsenic phosphorus: Switching p-type into high performance n-type semiconductor by arsenic substitution. *Nano-Micro Lett.* **2026**, *18*, 145.

[25] Chen, W. L.; Zhang, R.; Gu, M. Y.; Zhang, L. H.; Xie, B. H.; Yu, Z.; Chen, A.; Li, J. J.; Liu, S. Z.; Gao, P. Q. et al. An ultrahigh-contrast violet phosphorus van der Waals phototransistor. *Adv. Optical Mater.*

2024, *12*, 2301399.

[26] Kim, J.; Lee, B. H.; Choi, S. H.; Lee, J.; Lee, S.; Paul, K. K.; Kim, H.; Cho, B. W.; Ko, H.; Kim, J. W. et al. Phase-selective growth of violet phosphorus crystals via Sn–Bi flux. *ACS Nano* **2025**, *19*, 38499–38508.

[27] Zhang, L. H.; Gu, M. Y.; Li, L. R.; Zhao, X. W.; Fu, C. C.; Liu, T.; Xu, X. Q.; Cheng, Y. H.; Zhang, J. Y. High yield synthesis of violet phosphorus crystals. *Chem. Mater.* **2020**, *32*, 7363–7369.

[28] Thurn, H.; Krebs, H. Crystal structure of violet phosphorus. *Angew. Chem., Int. Ed.* **1966**, *5*, 1047–1048.

[29] Zhang, L. H.; Li, X. B.; Yao, F. F.; Li, L. R.; Huang, H. Y.; Zhao, X. W.; Liu, S. H.; Cheng, Y. H.; Xu, H.; Zhang, J. Y. Fast identification of the crystallographic orientation of violet phosphorus nanoflakes with preferred in-plane cleavage edge orientation. *Adv. Funct. Mater.* **2022**, *32*, 2111057.

[30] Cho, B. W.; Lee, J.; Kim, J.; Cha, W.; Rho, H.; Kim, K. K. Observation of low-frequency vibrational modes in anisotropic 2D violet phosphorus. *Adv. Funct. Mater.* **2025**, *35*, e10952.

[31] Katiyar, A. K.; Choi, J.; Ahn, J. H. Recent advances in CMOS-compatible synthesis and integration of 2D materials. *Nano Converg.* **2025**, *12*, 11.

[32] Shin, M.; Kim, J. H.; Ko, J. Y.; Haidari, M. M.; Jang, D. J.; Lee, K.; Kim, K.; Kim, H.; Park, B. H.; Choi, J. S. Excimer-ultraviolet-lamp-assisted selective etching of single-layer graphene and its application in edge-contact devices. *Nano Converg.* **2024**, *11*, 34.

[33] Sohn, A.; Moon, H.; Kim, J.; Seo, M.; Min, K. A.; Lee, S. W.; Yoon, S.; Hong, S.; Kim, D. W. Band alignment at Au/MoS_2 contacts: Thickness dependence of exfoliated flakes. *J. Phys. Chem. C* **2017**, *121*, 22517–22522.

[34] Wang, H. P.; Cai, S. X.; Liu, Z. F.; Sun, Y. L.; Xie, D. First-principles insights into the tuning mechanisms of electronic transport in violet phosphorene via defect and dopant engineering. *J. Phys. Chem. C* **2026**, *130*, 4177–4183.

[35] He, Q. Y.; Wang, D. D.; Qiu, H. X.; Si, N.; Yuan, Q. L.; Wang, R.; Liu, S. Y.; Wang, Y. M. Highly air-stable N-doped two-dimensional violet phosphorus with atomically flat surfaces. *ACS Nano* **2025**, *19*, 427–438.

[36] Liu, H.; Si, M. W.; Deng, Y. X.; Neal, A. T.; Du, Y. C.; Najmaei, S.; Ajayan, P. M.; Lou, J.; Ye, P. D. Switching mechanism in single-layer molybdenum disulfide transistors: An insight into current flow across Schottky barriers. *ACS Nano* **2014**, *8*, 1031–1038.

[37] Ahmed, F.; Choi, M. S.; Liu, X. C.; Yoo, W. J. Carrier transport at the metal-MoS_2 interface. *Nanoscale* **2015**, *7*, 9222–9228.

[38] Song, J.; Lee, S.; Seok, Y.; Ko, Y.; Jang, H.; Watanabe, K.; Taniguchi, T.; Lee, K. Drain-induced multifunctional ambipolar electronics based on junctionless MoS_2. *ACS Nano* **2024**, *18*, 4320–4328.

[39] Li, X. X.; Fan, Z. Q.; Liu, P. Z.; Chen, M. L.; Liu, X.; Jia, C. K.; Sun, D. M.; Jiang, X. W.; Han, Z.; Bouchiat, V. et al. Gate-controlled reversible rectifying behaviour in tunnel contacted atomically-thin MoS_2 transistor. *Nat. Commun.* **2017**, *8*, 970.

[40] Bai, Z. Q.; Xiao, Y.; Luo, Q.; Li, M. M.; Peng, G.; Zhu, Z. H.; Luo, F.; Zhu, M. J.; Qin, S. Q.; Novoselov, K. Highly tunable carrier tunneling in vertical graphene-WS_2-graphene van der Waals heterostructures. *ACS Nano* **2022**, *16*, 7880–7889.

[41] Lee, K.; Ngo, T. D.; Lee, S.; Shin, H.; Choi, M. S.; Hone, J.; Yoo, W. J. Effects of oxygen plasma treatment on Fermi‐level pinning and tunneling at the metal-semiconductor interface of WSe_2 FETs. *Adv. Electron. Mater.* **2023**, *9*, 2200955.

This is an open access article under the terms of the Creative Commons Attribution 4.0 International License (CC BY 4.0, https://creativecommons.org/licenses/by/4.0/).

© The Author(s) 2026. Published by Tsinghua University Press.